

Notes on the structure of radiotherapy depth-dose distributions

David W O Rogers

Carleton Laboratory for Radiotherapy Physics
Physics Department, Carleton University, Ottawa, Canada

drogers at physics.carleton.ca

Last edited 2014-01-24 10:21:16-05

©D.W.O. Rogers ¹

CLRP Report_CLRP_07_01

Contents

I	Introduction	2
II	Photon beam depth-dose distributions	2
II.A	Dose buildup in a 1.25 MeV parallel beam	4
II.B	Field size effects from a pure photon beam	5
II.C	Surface dose in pure photon beams	8
II.D	Field size effects on d_{\max} in realistic photon beams	10
II.E	Effects of SSD on pure photon-beam depth-dose curves	11
II.F	The dose/kerma and dose/ collision kerma ratios	12
II.G	Mean energy off-axis in incident photon beams	14
II.H	Mean energies in-phantom from photon beams	16
III	Electron beam depth-dose distributions	18
III.A	Field size effects with electron beams	19
III.B	Physics of electron depth-dose curves	21
III.C	Effects of SSD on electron depth-dose curves	25
IV	Relative dose in electron and photon beams	26
IV.A	Dose and kerma per unit incident fluence	27
V	Equivalent squares	29
V.A	Rectangular fields	29
V.B	Circular fields	31
VI	Effects of bin size on Monte Carlo calculated depth-dose curves	32
VI.A	Problems	32
	References	33

¹These notes, and other similar ones (see <http://www.physics.carleton.ca/~drogers/pubs/papers/#notes>), have been written for a graduate course I give in radiotherapy physics. You are hereby given permission to use these notes for non-commercial teaching or learning purposes and you are free to copy and distribute one or more copies as long as it is copied in its entirety, including this notice. These notes may not be placed on the internet, rather a link to the above site should be given.

I would be grateful for having my attention drawn to typos and/or mistakes or things which are not clear since these notes are a work in progress.

I Introduction

I have done a series of Monte Carlo calculations to elucidate various features of electron and photon beams used for radiotherapy. The calculations are to clarify certain issues and are unrealistic. In particular, calculations are often for parallel beams with no variation in fluence with field size and thus are demonstrating phantom effects only. Effects of beam contamination are important and mentioned in the text. Calculations are done using DOSRZnrc, CAVRZnrc or FLURZnrc,¹ user-codes for the EGSnrc Monte Carlo system for simulating electron and photon transport.^{2,3}

II Photon beam depth-dose distributions

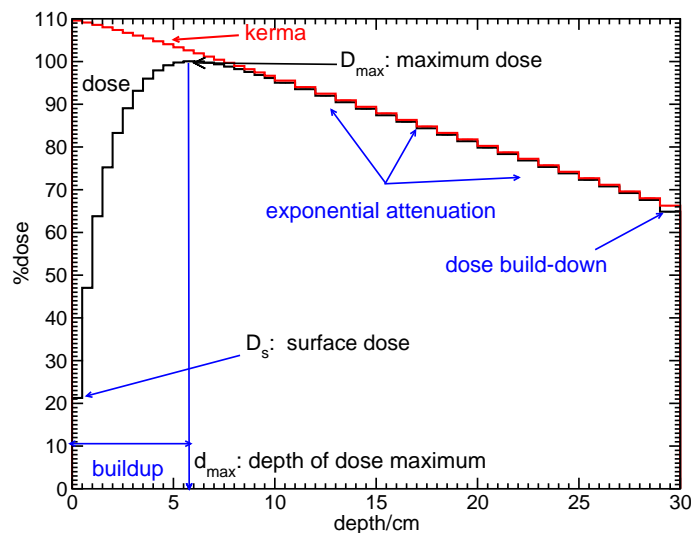


Figure 1: A photon depth-dose curve (high energy).

Fig 1 shows the central axis depth-dose curve for a high-energy photon beam incident on a water phantom (calculated for a broad 24 MV parallel beam with no electron contamination). Also shown is the kerma to water in the phantom. The essential features are as follows:

buildup region: The buildup region occurs because, for higher-energy photon beams, the secondary electrons travel some distance into the phantom as they deposit energy. Until transient charged particle equilibrium is reached, the dose continues to build up since more electrons are being added at each depth from the photon interactions. Past the dose maximum there is a transient charged particle equilibrium and as new particles are created, particles created upstream come to the end of their range. The thickness of the buildup region depends on the range of electrons created (see below about d_{\max}).

D_{\max} **and** d_{\max} : The value of the maximum dose, D_{\max} , occurs at depth d_{\max} . It occurs more deeply for higher-energy beams and corresponds roughly to the range of the

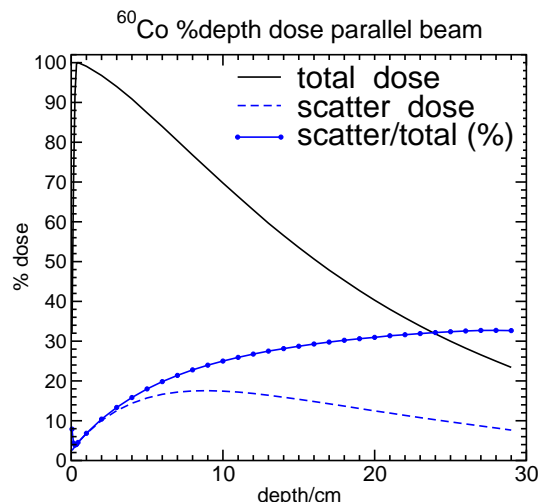


Figure 2: Scatter component of the dose as a function of depth in a $10 \times 10 \text{ cm}^2$ ^{60}Co beam.

highest energy knock-on electrons. Photon beam effects cause the position, d_{max} , to depend only slightly on the field-size (see section II.B) but in realistic beams d_{max} is strongly dependent on field size because of electron contamination which contributes dose which drops off rapidly from the surface. For larger field sizes there is considerably more electron contamination and therefore the d_{max} decreases with increasing field size. The dose maximum, D_{max} , increases with field size because of a combination of phantom scatter effects (see section II.B) and increased head-scatter from the source (quantified in the collimator factor)

attenuation region: past D_{max} the dose decreases because of the underlying attenuation of the photon beam and $1/r^2$ effects. There is an exponential attenuation of the primary beam (although for small values of μx , $e^{-\mu x} = 1 - \mu x$, i.e. it is close to linear). At the same time scattered photons are building up (see figure 2). The amount of scatter depends on the field size, there being more scatter for larger beams. This is discussed in section II.B. As well as the scatter building up with depth, there is a beam hardening effect which also causes the effective attenuation coefficient to change. In addition, the SSD of the beam affects the depth-dose curve. As the SSD decreases, the beam drops off more quickly because of the $1/r^2$ effects. Given the interplay of these 3 effects (scatter buildup, $1/r^2$ drop-off and beam-hardening), it is surprising that the depth-dose curves still drop off with an effective attenuation coefficient.

build-down region: There is a small, short range ‘build-down’ effect near the exit surface of the phantom caused by the lack of back scatter from the air compared to phantom material. Note that the kerma does not exhibit this build-down effect as much as the dose indicating that much of the missing backscatter dose is from electron backscatter.

electron contamination effects: These are not shown in figure 1 but in all realistic beams there is electron contamination from the source capsule (^{60}Co), the collimating system, intervening air and most importantly the flattening filter in accelerator beams.

This affects the buildup region and increases with increasing field size and is more important for high-energy beams. As mentioned above, this affects d_{\max} .

$1/r^2$ effects: in a beam from a point source, since the underlying photon fluence drops off as $1/r^2$ where r is the distance from the source, the resulting depth-dose curve is affected by this (and there are standard formulae for converting percentage depth-dose curves from one SSD to another). The farther the source is away, the more slowly the dose drops off.

surface dose: For megavoltage photon beams the surface dose is lower than the maximum dose. This skin sparing effect is due to the buildup phenomenon. However, quantitative statements about the surface dose are complex because of the sharp dependence on the thickness of the region included in the dose, the important role of contaminant electrons and the difficulty of making accurate surface measurements. See section II.C for more discussion.

II.A Dose buildup in a 1.25 MeV parallel beam

In figure 4.7 of his textbook,⁴ Herb Attix shows d_{\max} as occurring at approximately the point where the the dose curve (in a clean beam) crosses the kerma curve in the phantom and that transient charged particle equilibrium is established at the depth “equal to the maximum depth distance the secondary charged particles starting at the surface can penetrate in the direction of the incident rays”. To explore these statements, figure 3 shows a series of calculations done for a ^{60}Co beam. Various points are worth making. The dose maximum is achieved at slightly less than 0.5 g/cm^2 which is consistent with the maximum range of the highest energy electrons generated at the surface of the phantom as shown by the depth-dose curve for the 1.038 MeV electrons or the energy deposition kernel in the forward direction,⁵ both of which drop to zero by 0.5 g/cm^2 depth. At this depth the dose and kerma curves are parallel and hence this is the shallowest depth at which transient charged particle equilibrium can be said to exist. There is further discussion of the difference between the dose and kerma curves below. However, in contrast to Attix’s assertion, the dose maximum is not achieved where the kerma and dose curves cross, but somewhat past that point. Also, the dose does not equal either the kerma or the collision kerma since there is never true charged particle equilibrium. Note that the difference between the kerma and collision kerma curves is about 0.3%, consistent with the value of \bar{g} .

Figure 3 also shows a depth-dose curve calculated for the case in which primary photons are not attenuated (*i.e.*, they are replaced by an identical photon after they interact) and in which all scattered photons are eliminated and do not deposit any energy. This depth-dose curve demonstrates that the dose maximum is achieved at the same depth in this situation as in the more realistic simulation and hence dose maximum could not be at the point where the kerma intersects the dose curve. An interesting feature of this curve is the fact that dose maximum without any scatter or attenuation included is 2.6% less than when it is included, *i.e.*, the scatter effects dominate over the attenuation effects up to about 1.6 cm where the dose with scatter and attenuation falls below the dose with no scatter nor attenuation.

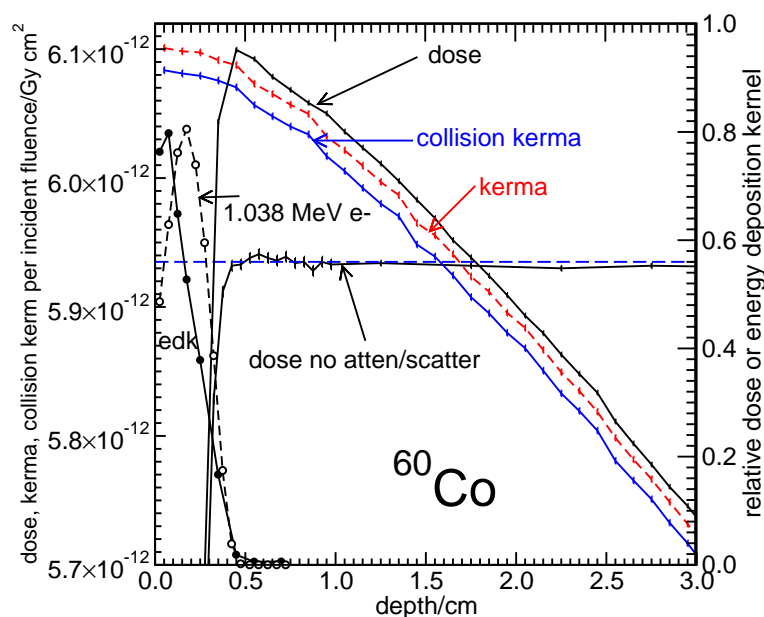


Figure 3: Depth-dose, depth-collision-kerma and depth-kerma curves for 10×10 cm^2 parallel 1.25 MeV photon beams incident on a water phantom. In addition, there is a depth-dose curve for which there is no attenuation of the photons with depth, nor any scatter. Note the left scale for the dose and kerma curves is offset significantly. The two curves with symbols starting at 0 and stopping around 0.5 cm are a forward going energy deposition kernel for a 1.25 MeV photon⁵ (solid line) and a depth-dose curve for a 1.038 MeV broad beam of electrons. The highest energy electron created by a 1.25 MeV photon is 1.038 MeV. Note that these last two curves use the right hand axis.

II.B Field size effects from a pure photon beam

To study the field size effects from a pure photon beam, calculations were done for a ^{60}Co and a 24 MV beam. The incident beams were parallel and done for a variety of beam radii.

Figures 4 and 5 show the dose per unit incident fluence as a function of depth for beams of different energies. The increase in dose at a given depth for larger fields is due to increased photon scatter from the larger volume of phantom irradiated by the larger beam. The increase is greater at lower energies because photons scatter to larger angles at these energies.

Note that the absolute dose rates per unit incident fluence vary considerably between the two beams. The variation in D_{max} with field size is shown quantitatively in figures 6 and 7 for the same two beams. What is shown here is entirely due to ‘phantom scatter’ effects since the incident beams are pure photon beams and the results shown are in terms of dose per unit fluence. In realistic beams there are additional increases due to the increased collimator scatter as the beam size increases (and taken into account with the collimator scatter factor).

Figures 8 and 9 show the percentage depth-dose curves for these same two beams. In these cases the difference in the absolute dose normalization is removed and one can see the differences in the attenuation portion of the depth-dose curve as a function of field size. It is clear that there is much more variation in the lower-energy beam because of the increased photon scatter contribution.

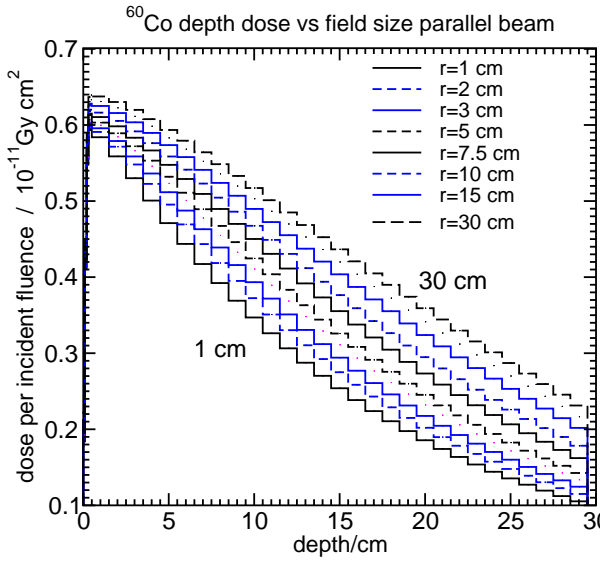


Figure 4:

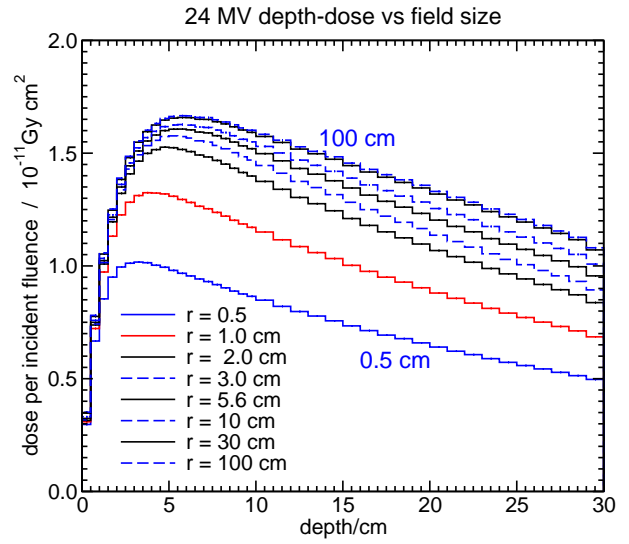


Figure 5:

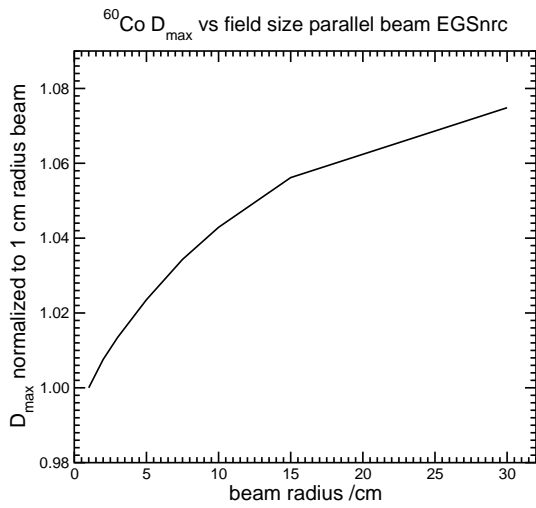


Figure 6:

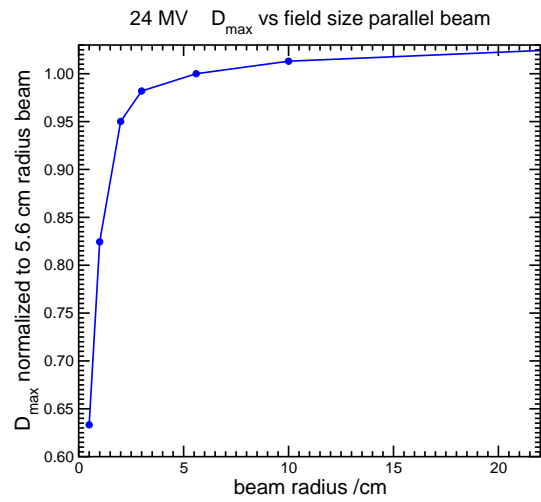


Figure 7:

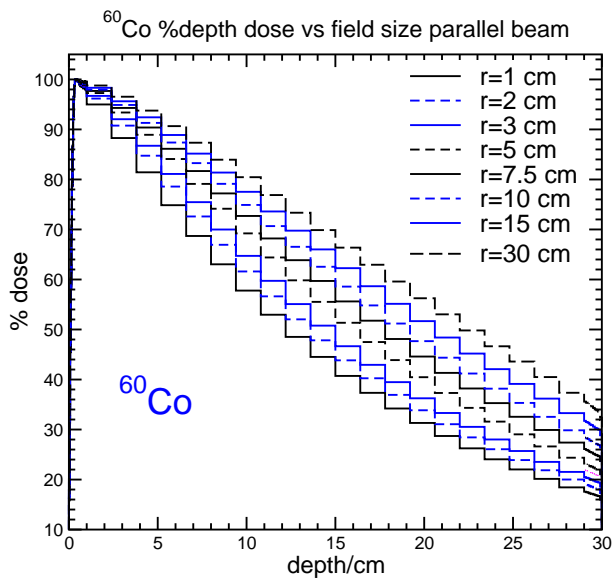


Figure 8:

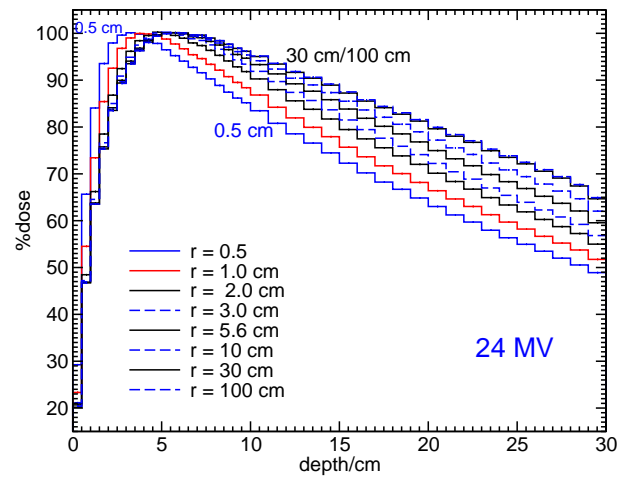


Figure 9:

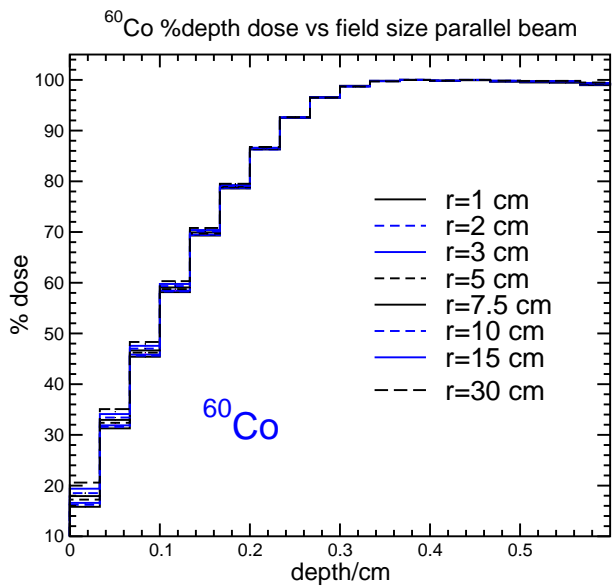


Figure 10: Discussed next page

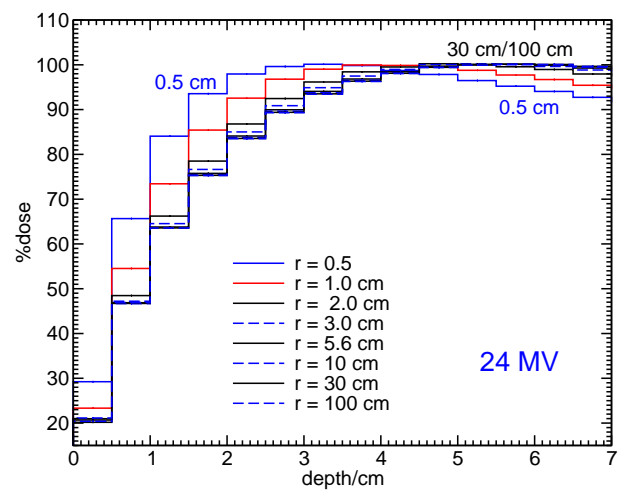


Figure 11:

II.C Surface dose in pure photon beams

As mentioned above, the surface dose in a photon beam is a complex quantity to consider and to measure.

It is commonly stated that the surface dose is lower in higher-energy photon beams than in lower-energy beams and experimentally, this is what is observed (with the caveat that these measurements are difficult).

However, this is not so clear from the calculations. Figures 10 and 11 show that the surface dose calculated is roughly the same for a ^{60}Co beam and a 24 MV beam as long as the curves are calculated using bins which are the same size relative to the thickness of the buildup region. This is more clearly evident in figure 12 where the two curves are plotted on the same graph for a 5 cm radius beam. Note that the x-axis has been normalized to the depth of dose maximum, d_{max} . It is clear that the two buildup curves are almost identical. Figure 13 shows the ^{60}Co beam buildup region calculated for 1 mm bins. In this case the ‘surface dose’ is around 32% rather than the 17% shown in figure 12, so clearly the calculated surface dose depends on the thickness of the scoring region in the calculations, or the thickness of the detector in a measurement.

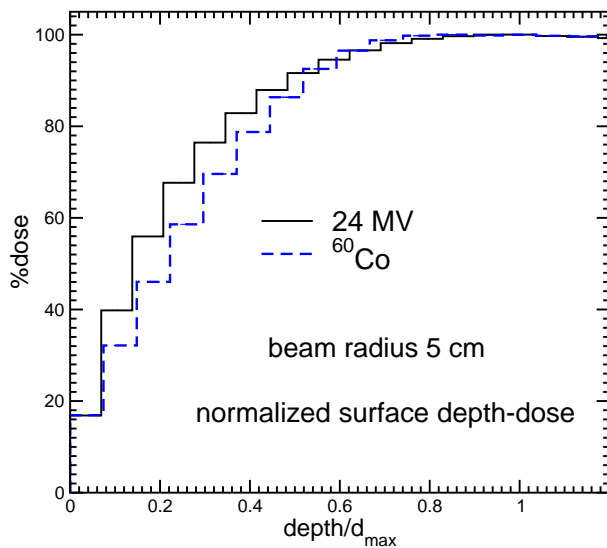


Figure 12:

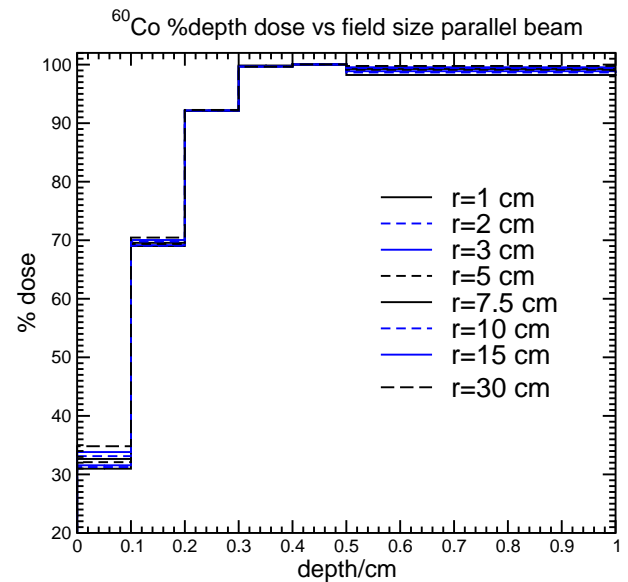


Figure 13:

Several other calculations were done to further elucidate the surface dose. The results are summarized in table I. Calculations were done for thin slabs of water, free in space, to show how much of the dose in the surface region was due to phantom backscatter. The DOSRZnrc user-code calculates the contribution of dose due to photons which scatter at least once in the phantom, including in the first slab, before interacting a second (or further) time and depositing energy in the surface region. For the 1 mm wide bin in a ^{60}Co beam, a comparison of the dose per unit fluence in the slab free in space ($16.94 \cdot 10^{-13} \text{Gy}\cdot\text{cm}^2$) vs the dose per unit fluence when there is a phantom ($22.24 \cdot 10^{-13} \text{Gy}\cdot\text{cm}^2$), shows that 76% of the dose per unit fluence comes from interactions in the bin itself and another significant component ($4.25 \cdot 10^{-13} \text{Gy}\cdot\text{cm}^2 = 19\%$) comes from scattered photons which means that only a small component ($22.24 - 16.94 - 4.25 = 1.05 = 4.7\%$) comes from backscattered

electrons from the primary photons. The corresponding numbers in the thinner, 0.333 mm, bins are 8.10=61.4%, 4.093=31.0% and 0.997=7.6%. The results for the 4 mm bins in the 24 MV beam are very similar: mostly from interactions in the bin itself (25.23=87%), backscattered photons and electrons contributing at most 28.96-25.23 = 3.73 = 13%. For the 1 mm bins in the 24 MV beam the numbers are interactions in the slab (8.41=70%), photon backscatter(2.46=20%) and backscattered electrons from primary photons(1.16=10%).

Table I: Doses per unit incident fluence (in units of ($10^{-13}\text{Gy}\cdot\text{cm}^2$) in water slabs of different thicknesses, both free in space and on the surface of a water phantom. The scatter dose is defined as any dose delivered after the primary photon has interacted at least twice and can include backscattered electrons or photons. Note that the kerma includes a contribution from backscattered photons. The results are for the broad incident beams although there is little variation with field size, especially for the slabs.

dose in slabs of water				
^{60}Co				
24 MV				
slab free in space				
slab thickness	0.033 cm ^a	0.1 cm	0.4 cm ^a	0.1 cm
dose	8.100	16.94	25.23	8.41
scatter dose	0.079	0.239	0.45	0.12
kerma	59.50	59.75	179.4	178.9
dose/kerma	0.14	0.284	0.14	0.047
slab on phantom				
slab thickness	0.033 cm ^a	0.1 cm	0.4 cm ^a	0.1 cm
dose	13.19	22.24	28.98	12.03
scatter dose	4.093	4.25	N/A	2.46
kerma	63.39	63.68	180.5	181.0

^aThese thicknesses correspond to $d_{\text{max}}/14$, the bin sizes shown in the figures above.

For a more detailed discussion of the buildup region for ^{60}Co beams, see ref.⁶

II.D Field size effects on d_{\max} in realistic photon beams

In the previous section we examined the effects of field size in pure photon beams. However, in realistic beams the electron contamination changes (increases) as the field size increases and this affects D_{\max} and d_{\max} . Sixel and Podgorsak⁷ did an elegant study of this effect. Figure 14 shows the depth of dose maximum, d_{\max} as a function of the size of a square beam for 3 different photon beam qualities. As expected, d_{\max} increases for higher energy beams. But the depth of dose maximum first increases with field size (as seen in fig 9), reaches a maximum at something less than $5 \times 5 \text{ cm}^2$ field sizes and then decreases as the field size increases further.

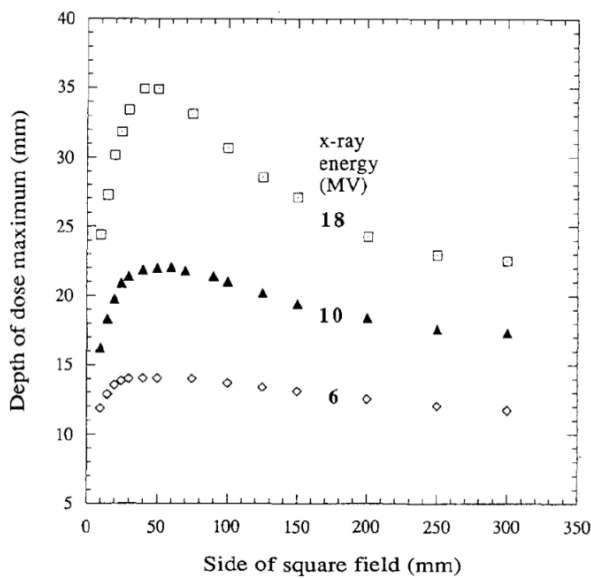


Figure 14: Fig 1 from Sixel and Podgorsak.⁷

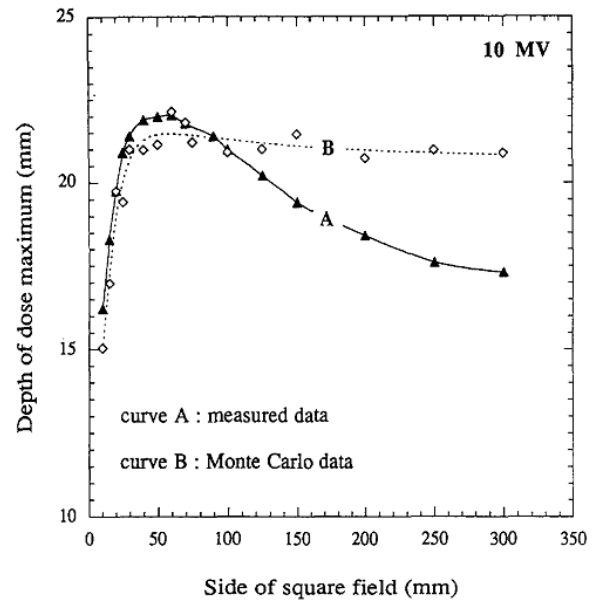
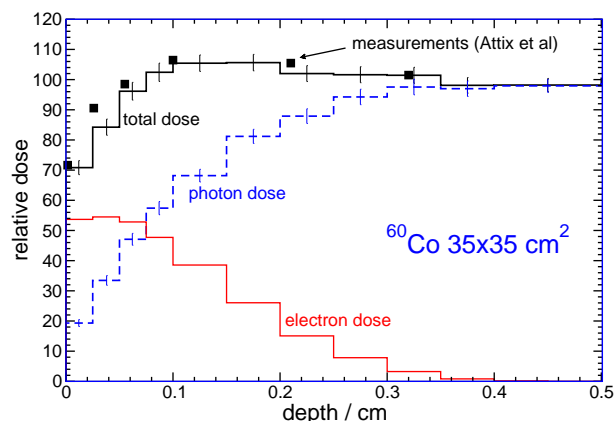
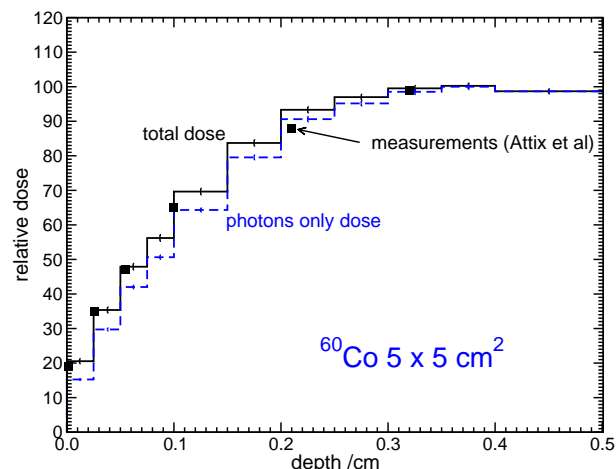


Figure 15: Figure 2 from Sixel and Podgorsak.⁷

Figure 15 shows the same curve again for the 10 MV beam (curve A) but also shows a Monte Carlo calculated curve which shows the same depth of dose maximum vs field size but for a pure 10 MV photon beam. It can be seen clearly that the initial increase in d_{\max} for small field sizes is due to the photon beam alone but past about $5 \times 5 \text{ cm}^2$ field sizes the photon component becomes constant (as seen in figure 9). The decrease must therefore be due to the electron contamination. Basically what is happening is that as the field size increases, the amount of electron contamination increases significantly and increases the dose near to the surface. The net effect is to cause the actual value of the dose maximum, D_{\max} , to increase while d_{\max} decreases.

Figures 16 and 17 demonstrate this effect for a ^{60}Co beam. In the $35 \times 35 \text{ cm}^2$ field the effect of the electron contamination is to move d_{\max} to 1.7 mm whereas for the $5 \times 5 \text{ cm}^2$ field there is virtually no electron contamination and the value of d_{\max} is more like 5 mm.

Figure 16: Based on ref.⁸Figure 17: Based on ref.⁸

II.E Effects of SSD on pure photon-beam depth-dose curves

Variation of SSD causes changes in the depth-dose curves. Some of this is due to changes in the electron contamination as the amount of photon interaction in the air occurs. There are also effects from the change in $1/r^2$. There are formulae available for correcting between various SSDs (see, *e.g.*, ref⁹).

Figure 18 shows the variation in ^{60}Co beam depth dose curves as the SSD varies from 70 cm to 400 cm. It is clear that this is a substantial effect which must be taken into account. The most important cause of the variation is the $1/r^2$ effect which is more dramatic for shorter SSDs. There is also a slight change in the scatter conditions as the SSD changes due to the increased volume of phantom which is irradiated for shorter SSD.

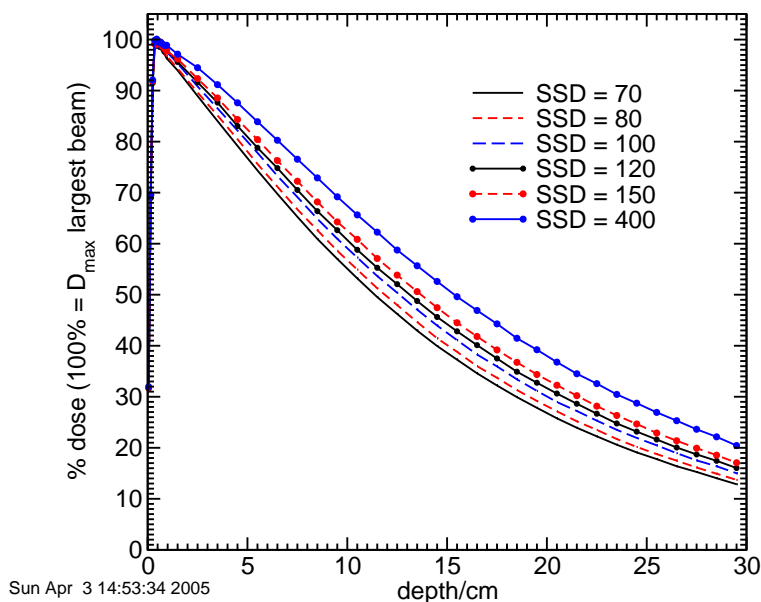


Figure 18: Variation in depth-dose curves in a ^{60}Co beam as the SSD is varied with a fixed field size of 100 cm^2 . Dose maximum for the largest SSD is taken as 100%.

II.F The dose/kerma and dose/ collision kerma ratios

Figure 3 on page 5 shows the dose being greater than the kerma and collision kerma in a ^{60}Co beam once past D_{max} . Figure 19 shows the dose, kerma and collision kerma for a 100 cm^2 24 MV parallel beam incident on a water phantom. Here the kerma is greater than the dose although the dose is greater than the collision kerma as expected from the approximation that $D = K_{\text{col}}(1 + \mu'\bar{x})$ in regions of transient charged particle equilibrium. In summary, for 24 MV, $K > D > K_{\text{col}}$, whereas for ^{60}Co , $D > K > K_{\text{col}}$.

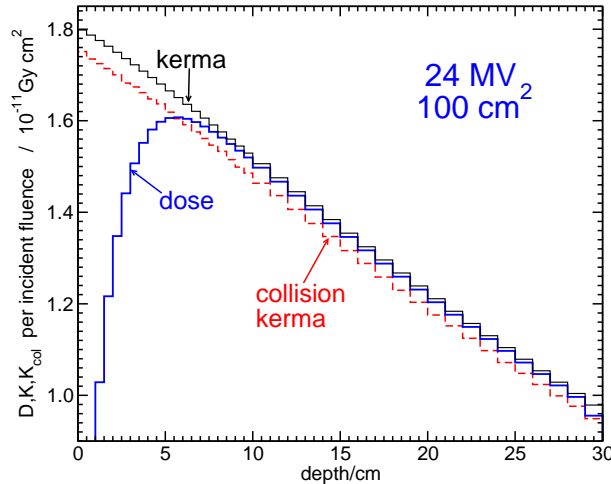


Figure 19:

The ratio of dose to collision kerma is usually denoted β .¹⁰ One can calculate this ratio with some accuracy and figures 22 and 23 show the values of β for 24 MV parallel photon beams incident on a water phantom as a function of depth and field size (although there is some bin size dependence on the values, bins are 5 mm deep up to 10 cm where they become 10 mm deep). As expected, the ratio is much less than unity at the surface until the dose builds up. The dose to kerma ratio (fig 21) grows to be slightly less than unity past the dose maximum whereas the dose to collision kerma ratio rises to about 2% greater than unity for fields of 100 cm^2 or more.

These calculated values for 24 MV show that the ratios β and dose/kerma are not very field size dependent except for small fields, and roughly constant past the dose maximum except for the small fields which decrease slightly with depth. For the small field sizes, the ratio is less because the field is so small that there is no lateral electron equilibrium on the central axis and hence the dose value falls short of the kerma value.

Figure 24 for a ^{60}Co beam shows that the ratio of dose to kerma does not depend very much on field size in the buildup region. Figure 25 shows that past dose maximum, the dose/kerma and dose/collision kerma ratios are almost completely flat although the dose/kerma ratio decrease slightly (0.05%) with depth for very large beams. Fig 25 implies that the difference between collision kerma and kerma is about 0.3%, consistent with the value of g in a ^{60}Co beam. This figure also shows that the calculated results depend on the bin sizes used in the calculations, the lower pair of results being for 2 mm thick bins everywhere whereas the upper pair of the dose/kerma ratios are for 10 mm depth bins. When one is looking at comparisons at the 0.1% level, bin size artifacts become important.

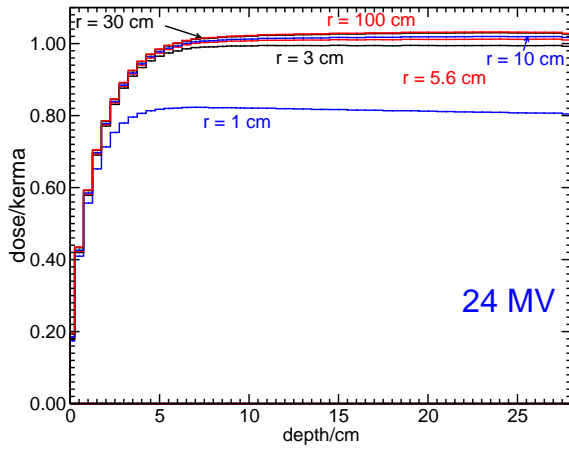


Figure 20:

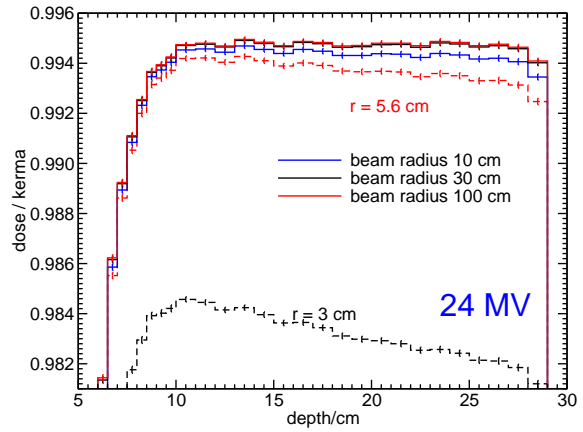


Figure 21:

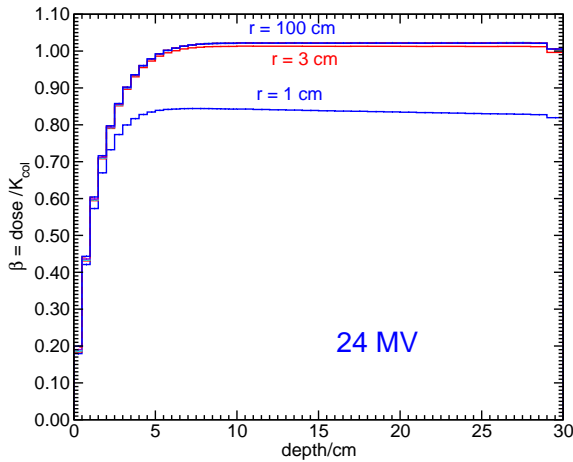


Figure 22:

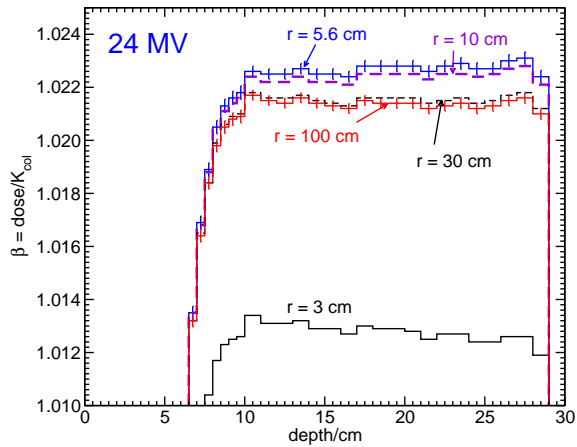


Figure 23:

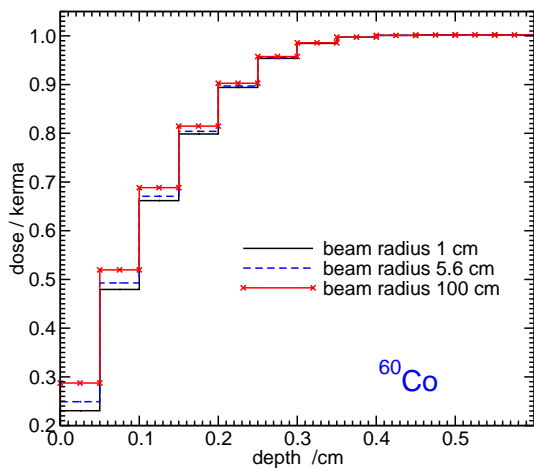


Figure 24:

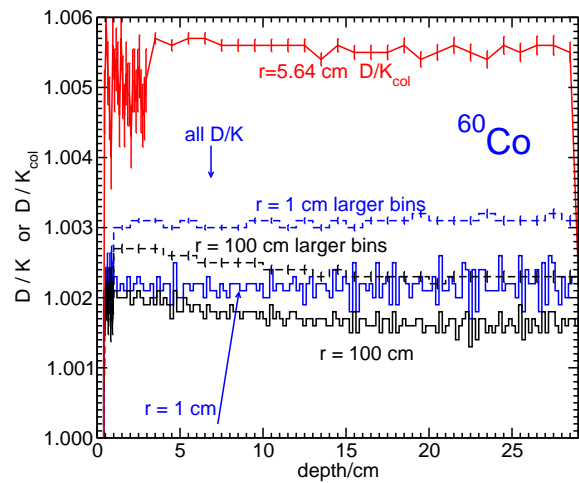


Figure 25:

II.G Mean energy off-axis in incident photon beams

Unlike the beams presented above, realistic photon beams vary both in intensity and average energy as a function of position away from the axis. Figure 26 shows the calculated mean energies as a function of position off-axis for 9 different broad ($40 \times 40 \text{ cm}^2$) beams from commercial accelerators.¹¹ It is clear that the effect of flattening filters is to considerably reduce the average energy off-axis (as opposed to the effects from scatter which do not change the average energy very much). Figure 27 shows similar results for $10 \times 10 \text{ cm}^2$ beams. In this case the direct photons which are outside the beam have passed through the jaws and therefore are heavily filtered and the average energy may go up substantially. However, the actual number of such photons is very low and the overall average photon energy outside the beam is determined by the energy of the scattered photons.

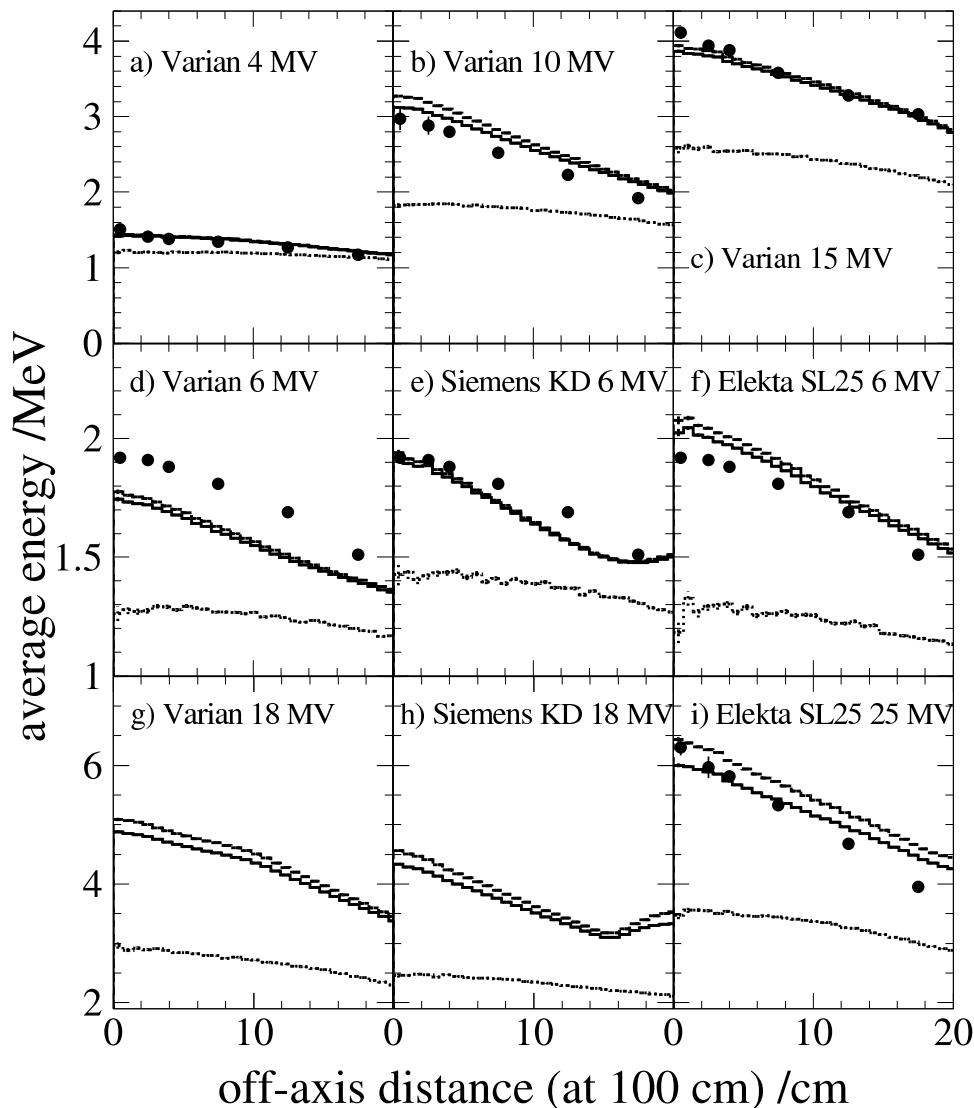


Figure 26: Calculated average (above 0.01 MeV) photon energies for large open fields at 100 cm, scored in annular bins, for square beams from commercial linacs. The filled circles are calculated by Mohan *et al.*¹² for Varian Clinacs. The three histograms represent average energies for: **all photons** (solid histograms), **direct photons** (dashed histograms, ie the upper of 2 apparently solid histograms), and **scattered photons** (dotted histograms). From ref¹¹

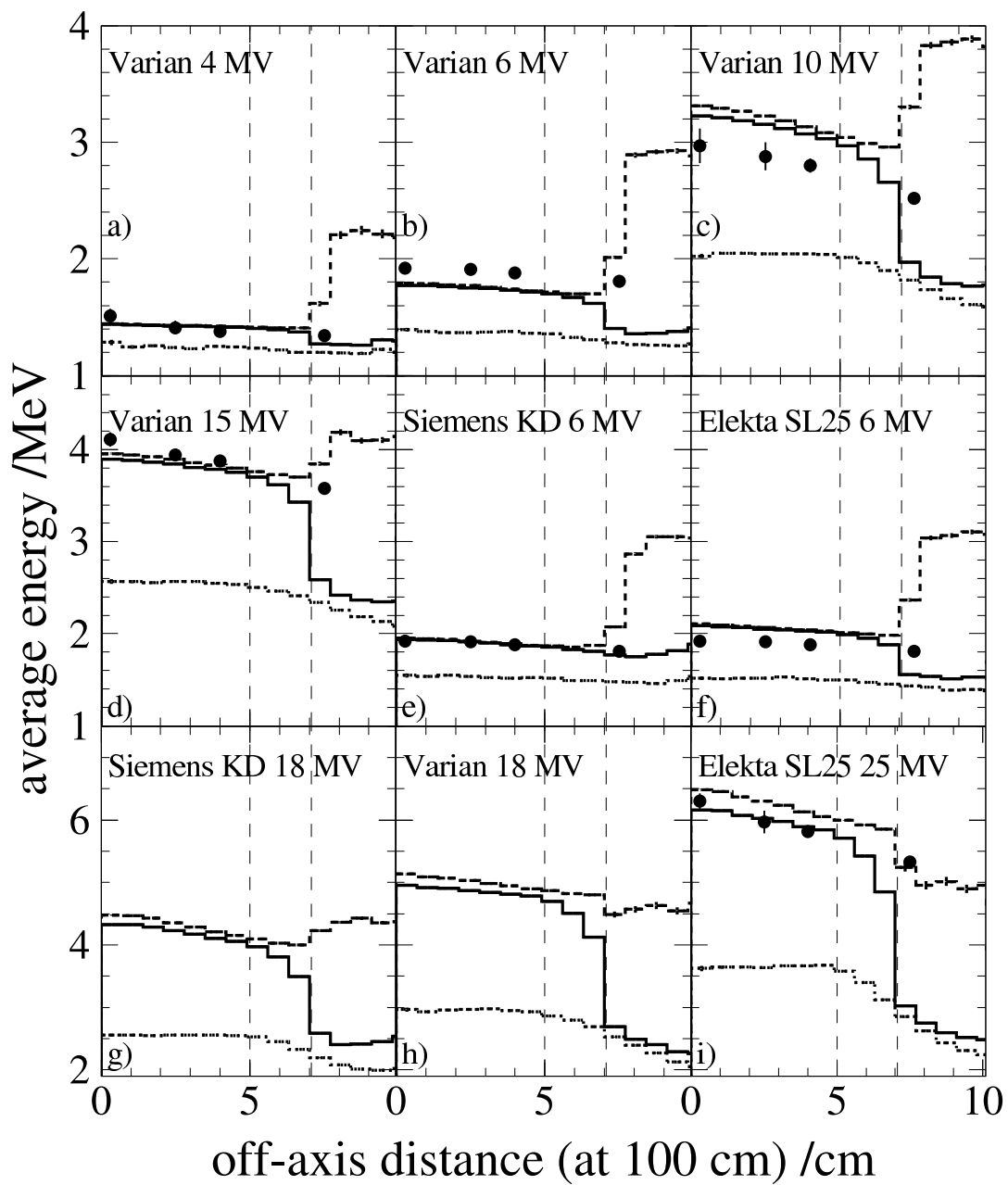


Figure 27: Same as previous figure except for $10 \times 10 \text{ cm}^2$ beams. The vertical dashed lines show the range of radii between which the edges of the square field reside.

II.H Mean energies in-phantom from photon beams

In the previous section the mean energy in the realistic beams from accelerators were presented. In this section we go back to some simple calculations in which a point source at 100 cm irradiates a water phantom and we ask, what happens to the mean energy in the phantom as a function of depth and radius? The initial spectra are from references^{11,13} and correspond to the 6 and 18 MV beams from Varian machines and that from a ^{60}Co unit. In all cases the spectra are for a $10\times 10\text{ cm}^2$ field although they are used for other sizes of beam in the present calculations.

Figure 28 shows the mean energies as a function of depth on the central axis of the water phantom. For the primary photons one can see a clear beam hardening with depth as the low-energy photons are preferentially scattered and absorbed. However, overall the photon average energy goes down as the number of low-energy scattered photons increases with depth. This effect is much more significant for the 21 cm radius beam than for the 100 cm^2 field size where there is relatively less scatter.

Note that the average energy of the primaries for the 6 MV beam at the surface is equal to the average energy shown in figure 27 for the Varian 6 MV beam ($\approx 1.69\text{ MeV}$). However, even right at the surface, the effect of the scattered photons is to significantly reduce the average photon energy, to 1.3 MeV for the broad beam or 1.5 MeV for the smaller beam size.

It is interesting that the average energy of the electrons is actually higher than that of the photons at depth. For the average energy of electrons above 189 keV (ie ECUT = 700 keV), this is partially an artifact of the different cut-offs used for electrons and photons in the calculations. However, as seen when the threshold for inclusion in the average energy is 10 keV, the average energy of the electrons is still greater than that of the photons at depth. There is some discussion below of a similar situation related to the average electron and photon energies in the bremsstrahlung tail in electron beams (see discussion of fig 40, page 24).

Figure 29 shows the average energies as a function of radial position at 10 cm depth in a broad($r=21\text{ cm}$) 6 MV beam. Recall that unlike figure 26, the incident beam in this case has a uniform incident average energy and all the effects seen are due to in-phantom scatter. The average energies of the primaries is constant with radial position. The average energy of all photons increases near the edge because the number of scattered photons is maximal on the central axis where photons are scattered from all directions whereas on the edge of the beam they are scattered from one side only.

The figures and discussion relate to 6 MV photon beams but calculations for ^{60}Co and 18 MV beams show similar trends.

Figure 30 shows the mean energy as a function of depth for parallel beams of the 6 MV beam for different field sizes. The lack of back-scattered photons at the back of the phantom for the larger fields leads to an increased average energy.

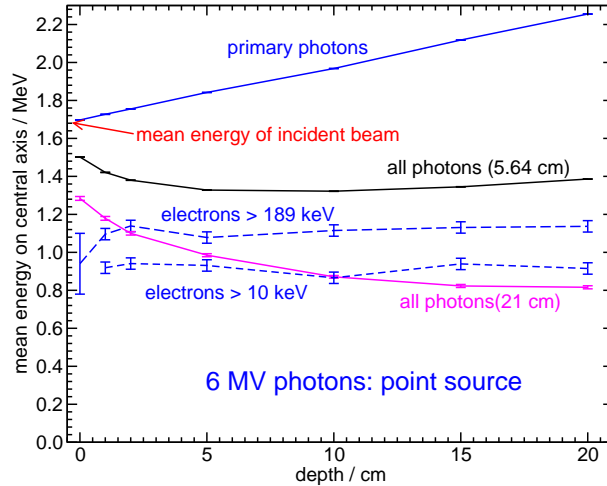


Figure 28: Mean energy (above 10 keV for photons and 189 keV or 10 keV for e⁻) on the central axis for different components of a uniform 6 MV photon beam from a point source at 100 cm incident on a water phantom with radii of 5.64 cm or 21 cm. The "all photons" cases depend strongly on the radius of the initial beam. For the other components (ie electrons and primary photons, there is virtually no dependence on the initial beam radius and only the broad beam results are shown.

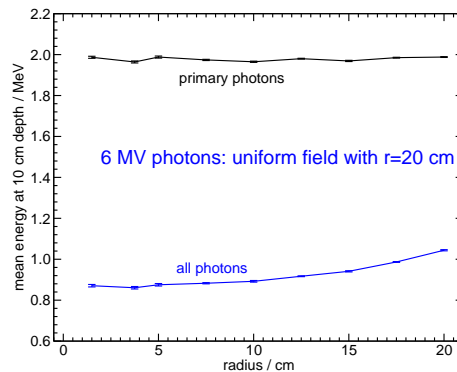


Figure 29: Average energies vs radial position at 10 cm depth in a uniform broad 6 MV beam from a Varian accelerator.

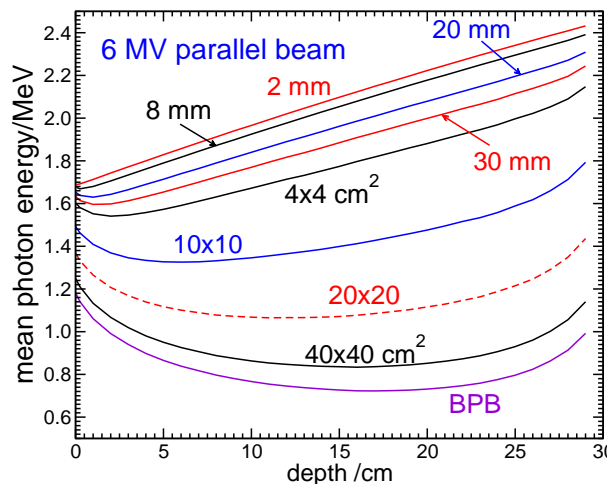


Figure 30: Average energy on-axis as a function of depth in a 30 cm thick phantom for different incident beam sizes for a 6 MV parallel beam incident.

III Electron beam depth-dose distributions

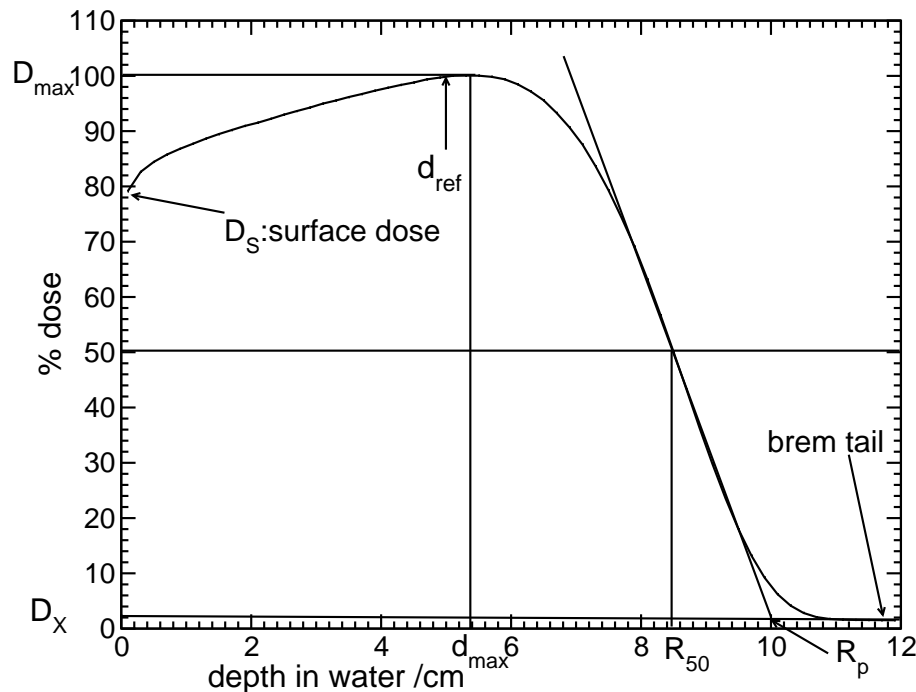


Figure 31: Standard elements of an electron beam depth dose curve as calculated for a mono-energetic 20 MeV electron beam at an SSD of 100 cm and an area of 100 cm². Note that for a realistic beam of this energy the bremsstrahlung tail would be more significant because in real beams the majority of the bremsstrahlung tail comes from the bremsstrahlung generated in the scattering foils and these photons are not included in this calculation where all we have is the bremsstrahlung generated in the phantom itself.

buildup to D_{max} : The major buildup in electron beams is due to the increasing electron fluence with depth as the electrons scatter in the phantom. The buildup is more pronounced for low-energy electrons because they scatter more.

surface dose: The surface dose relative to dose maximum is smaller for low-energy beams because of multiple scattering and hence the fluence and dose buildup is greater at low energies. However, the surface dose per unit incident fluence in all radiotherapy electron beams is given by $(\bar{L}/\rho)_{water}$ and hence is roughly the same since the restricted stopping power is roughly constant for all energies of use in clinical radiotherapy. There is a very shallow ‘buildup region’ of a few percent at most which is due to the buildup of secondary or knock-on electrons in the phantom. For realistic beams this already minor buildup may be negligible because of secondary electrons which are already part of the incident beam.

dose drop off: Electron beams drop off more or less rapidly after they reach D_{max} because the electrons have lost all of their energy and stop. This drop-off is the basis of their use in clinical practice. The practical range of the beam, R_p is defined as the intersection

of the tangent to the inflection point on the dose fall off region and the bremsstrahlung tail.

bremsstrahlung tail: The bremsstrahlung tail continues past R_p into the phantom and is mostly from bremsstrahlung which is incident on the phantom from the accelerator but also includes a small component from bremsstrahlung created in the phantom by the electron beam. The bremsstrahlung tail is much larger for higher-energy beams and for accelerators with thicker scattering foils. In fig 31 the bremsstrahlung is entirely that from within the phantom.

slope of fall-off region: The slope is due to the combination of energy loss straggling from bremsstrahlung and knock-on electron interactions, range straggling due to multiple scattering of the electrons and the energy distribution of the incident electron beam.

R_{50} : R_{50} specifies the depth at which the dose in the electron beam falls to 50% of dose maximum and is used to specify the beam quality in dosimetry protocols. R_{50} increases with increasing field size up to what is a broad beam and after that is constant. To first order R_{50} increases linearly with the mean incident electron energy ($E_o = 2.33R_{50}$) but there are some minor SSD variations as well.

output variations with field size: There is variation in the value of the maximum dose, D_{\max} , with field size but this is primarily a function of the accelerator's characteristics. There is some variation which is due to phantom effects, but this is not as important as in photon beams except for very small radii beams (see section III.A).

variation of d_{\max} with field size: the depth-dose curves for electron beams vary substantially for narrow beams because lateral equilibrium is not established at the greater depths yet (see section III.A). Thus d_{\max} moves closer to the surface for narrow beams. However, once lateral equilibrium is established, there is no further variation with increasing field size.

III.A Field size effects with electron beams

The following results are for parallel beams of electrons which show no variation with field size. In a real beam there is a distinct increase in output with increasing field size due to changes in the collimation system but here we concentrate on phantom effects.

Figures 32 and 33 demonstrate that there is little field size dependence in the output due to phantom effects for broad beams, *i.e.*, once the beam's radius is greater than some minimum (about 1 cm at 6 MeV and 5 cm at 20 MeV). A commonly used rule of thumb is that the electron beam can be considered broad if its diameter is larger than the practical range of the beam. On the other-hand, figures 34 and 35 demonstrate that the shape of the depth-dose curve does change dramatically for the narrow beams. In particular the depth of dose maximum, d_{\max} , decreases substantially for narrow beams because lateral equilibrium has not yet been established at the greater depths and the relative surface dose increases due to the drop off in the absolute value of the maximum dose.

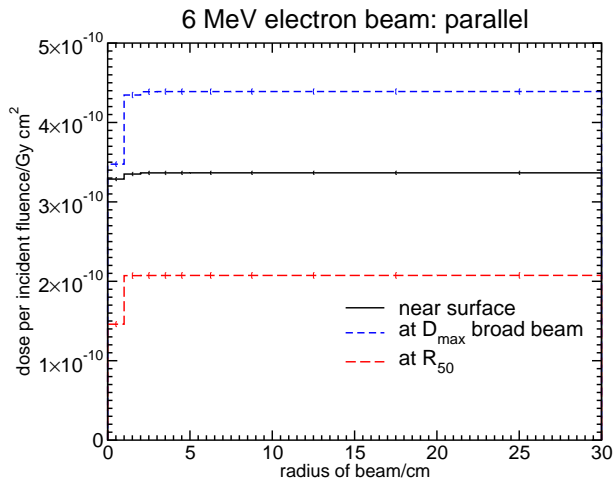


Figure 32:

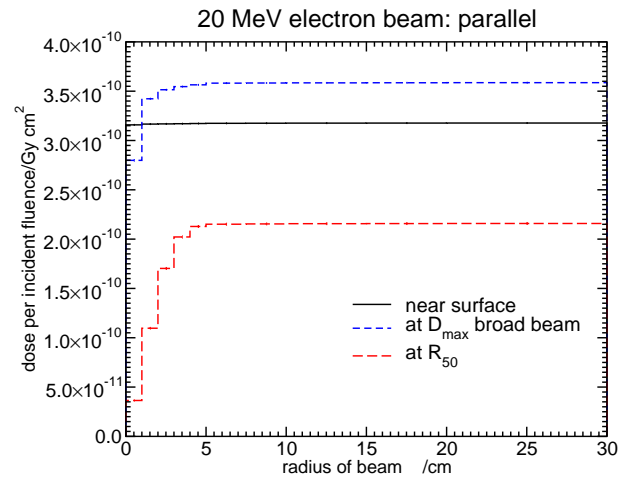


Figure 33:

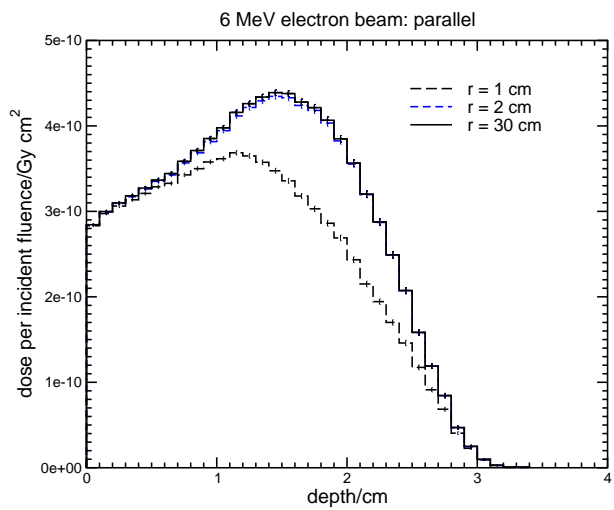


Figure 34:

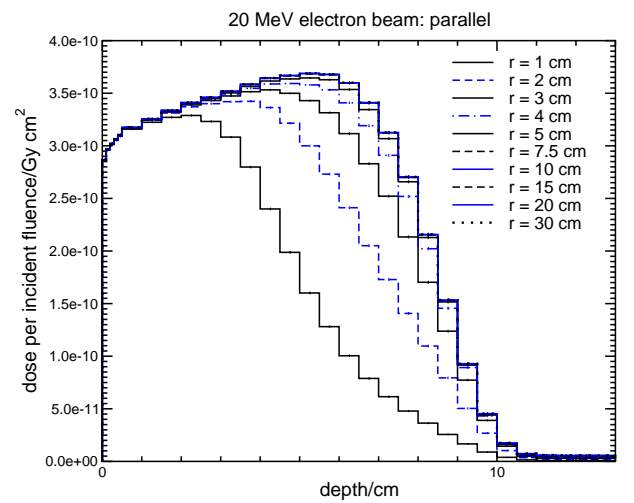


Figure 35:

III.B Physics of electron depth-dose curves

This section directly quotes material I wrote for a Chapter in the Erice Monte Carlo book.¹⁴

Fig. 36 presents two CSDA calculations (*i.e.* no secondaries are created and energy-loss straggling is not taken into account). For the histogram, no multiple scattering is modelled and hence there is a large peak at the end of the range of the particles because they all reach the same depth before being terminated and depositing their residual kinetic energy (189 keV in this case). Note that the size of this peak is very much a calculational artifact which depends on the width of the bin the histories terminate in. The other curve includes the effect of multiple scattering which leads to a lateral spreading of the electrons which thus shortens the depth of penetration of most electrons and an increase in the dose at shallower depths because the fluence has increased. In this case, the depth-straggling is entirely caused by the lateral scattering since every electron has travelled the same distance.

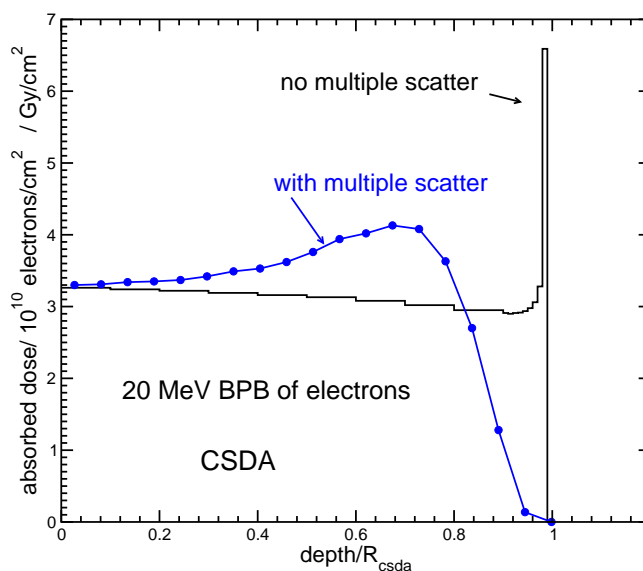


Figure 36: Depth-dose curve of broad parallel beam of 20 MeV electrons incident on a water phantom. The histogram is a CSDA calculation with no multiple scattering and the other curve is a CSDA calculation with multiple scattering included (but no energy straggling). From a figure in ref.¹⁴

Figure 37 presents three depth-dose curves calculated with all multiple scattering turned off - *i.e.* the electrons travel in straight lines (except for some minor deflections when secondary electrons are created). In the cases including energy-loss straggling, a depth straggling is introduced because the actual distance travelled by the electrons varies, depending on how much energy they give up to secondaries. Two features are worth noting. Firstly, the energy-loss straggling induced by the creation of bremsstrahlung photons plays a significant role despite the fact that far fewer secondary photons are produced than electrons - however they have a larger mean energy. Secondly, the inclusion of secondary electron transport in the calculation leads to a dose buildup region near the surface.

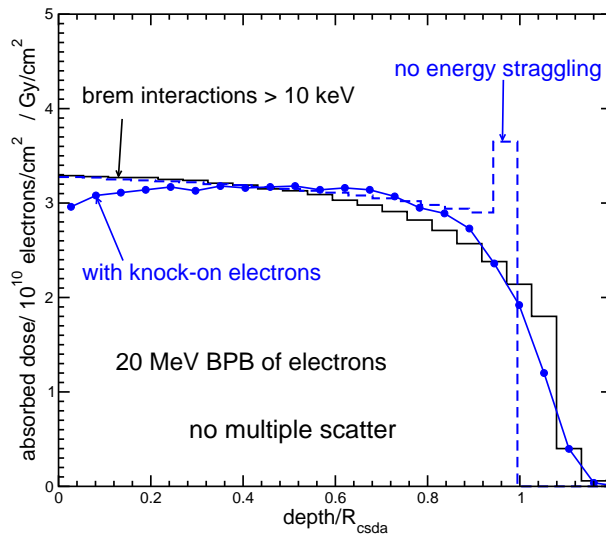


Figure 37: As in previous figure but in all cases there is no multiple scatter. The dashed curve includes no energy straggling and is thus the same case as the histogram in the previous figure (note that the height of the peak is dependent on the thickness of the depth bin). The solid histogram includes energy straggling due to creation of bremsstrahlung photons with energies above 10 keV whereas the curve with solid symbols includes energy straggling due to creation of knock-on electrons above 10 keV.

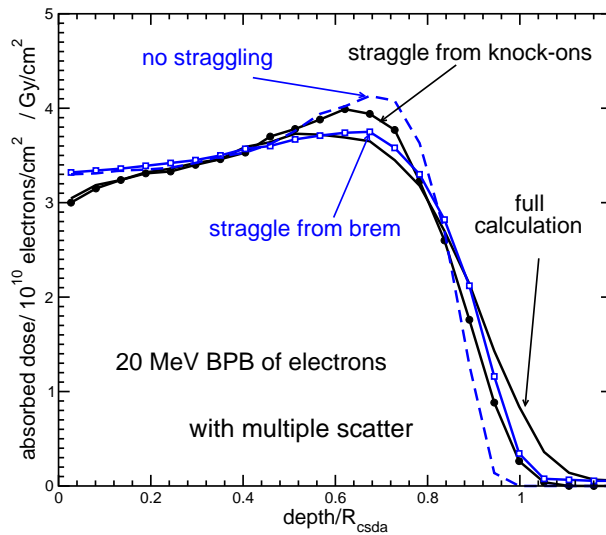


Figure 38: As in previous figure except that here there is multiple scattering in all cases. The dashed curve includes no energy straggling. The solid line with open squares includes only energy straggle from bremsstrahlung production and that with solid symbols includes energy straggling only from the creation of knock-on electrons. The solid curve with no symbols is the full calculation with both types of energy straggling included. From data in ref.¹⁴

Figure 38 presents a combination of the effects in the previous two figures. The extremes of no energy-loss straggling and the full simulation are shown to bracket the results in which energy-loss straggling from either the creation of bremsstrahlung or knock-on electrons is included. The bremsstrahlung straggling has more of an effect, especially near the peak of the depth-dose curve.

Figure 39 presents the calculated fluence vs depth and dose vs depth curves for a broad parallel beam of 9 MeV electrons on a water tank. The first observation is that despite the large fluence of photons, their contribution to the dose is very small as can be seen by the small dose values in the bremsstrahlung tail. There are four curves for the fluence. The calculations have been done with a cutoff for tracking secondary electrons of 521 and 711 keV (total energy, 10 keV and 200 keV kinetic energy). The total fluence varies noticeably depending on which cutoff is used, which indicates that there is a significant fluence of electrons between 10 and 200 keV kinetic energy in the beam. This makes the point that the fluence in an electron beam must always be specified in terms of the cutoff energy. The same applies if we talk of the average energy at a given depth. In the figure, the fluence of primary electrons for the two different cutoffs is seen to be nearly identical in each case which indicates that there are few primary electrons between 10 keV and 200 keV, although near the peak of the curves there is a slight difference between the curves.

Another important point raised by figure 39 is that the dose curve follows the fluence curves very closely. Thus the majority of the shape of the depth-dose curve comes from the variation in fluence with depth, not from the variation in stopping powers or any other features.

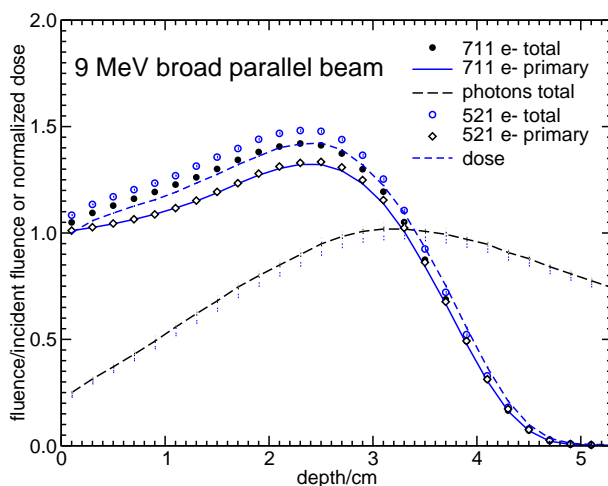


Figure 39: Calculated fluence vs depth in a water phantom irradiated by a broad parallel beam of 9 MeV electrons. The electron fluences are specified by the cutoff energy for electron transport. Also shown is the depth-dose curve in the same beam, normalized to unity in the first bin.

Figure 40 presents the average energy as a function of depth for the same 9 MeV beam as in the previous figure. Note that once past the practical range, the average energy of the electrons actually increases since these are being generated by the photons in the bremsstrahlung tail. There is an apparent contradiction in the sense that the average energy of the electrons is greater than that of the photons giving rise to them. I am not sure I understand this but it may be because of a very large number of very low-energy photons which affect the average photon energy but only generate very low-energy electrons which slow down and stop almost immediately and therefore do not contribute significantly to the electron fluence when they Compton scatter whereas the relatively few high-energy photons generate much higher energy electrons. This is because of the physics of Compton scattering whereby the fraction of energy transferred to electrons goes up rapidly with increasing photon energy (about 12% at 100 keV, *i.e.*, 12 keV vs over 60% at 6 MeV, *i.e.*, 3.6 MeV).

The figure also presents the Harder relationship¹⁵ for the mean energy at depth given by $\bar{E}_{ave} = E_0(1 - z/R_p) = 9.0(1 - z/4.5)$. See Ding et al¹⁶ for a more detailed discussion and comparisons for realistic beams.

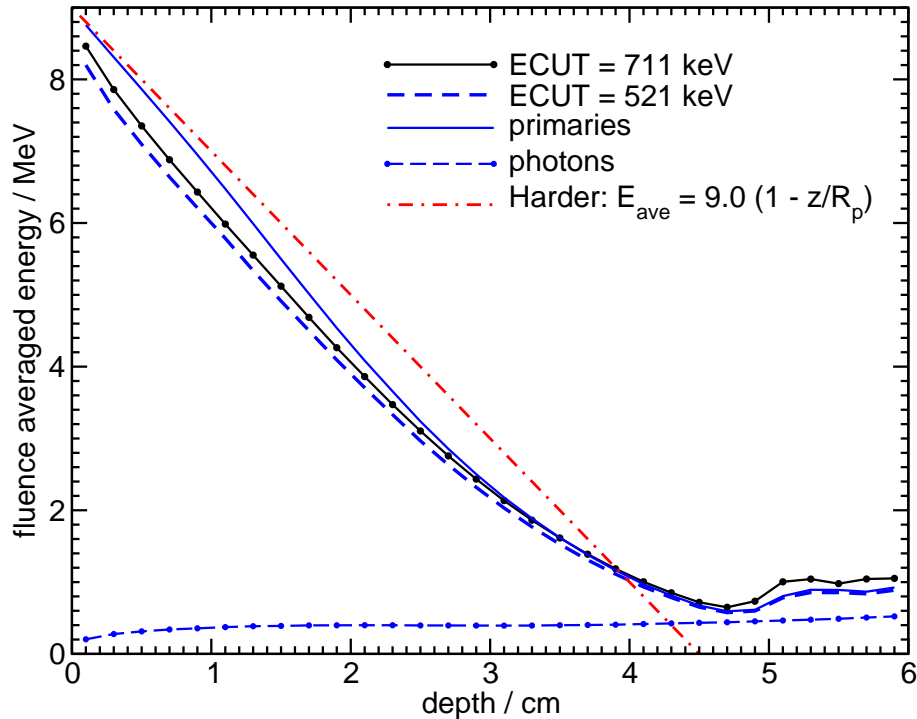


Figure 40: Average energy as a function of depth for a broad parallel beam of mono-energetic 9 MeV electrons incident on a water phantom. Note the increase in the average energy of the electrons at depth which is in the bremsstrahlung tail.

III.C Effects of SSD on electron depth-dose curves

As the SSD is varied, there are changes in the depth-dose curves from an electron beam, primarily, although not exclusively, from $1/r^2$ effects. Figure 41 shows the effects on a mono-energetic 20 MeV beams central-axis depth-dose curve as the SSD is varied from 80 cm to 400 cm.

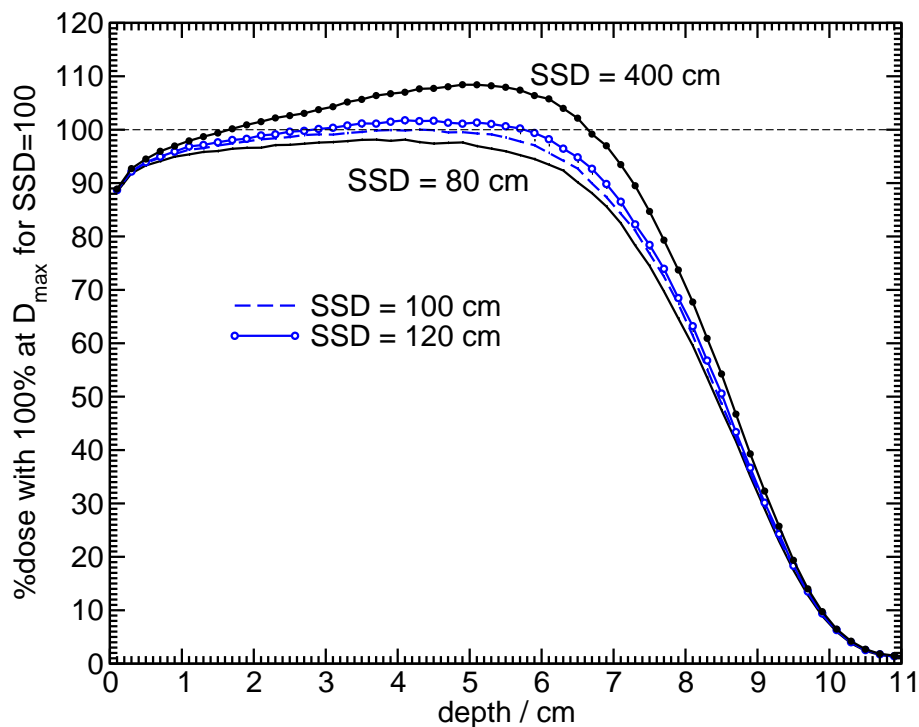


Figure 41: Variation in depth-dose curves in a 20 MeV electron beam as the SSD is varied with a fixed field size of 100 cm^2 . Dose maximum for the $\text{SSD} = 100 \text{ cm}$ beam is taken as 100%.

IV Relative dose in electron and photon beams

In a photon beam, in a region of transient charged particle equilibrium the dose is roughly equal to the kerma (see fig 1 or 3) and hence:

$$D_w = \Psi \left(\frac{\overline{\mu_{\text{en}}}}{\rho} \right)_{\text{water}} \quad (1)$$

where Ψ is the photon energy fluence. Thus:

$$\frac{D_w}{\phi} = E \left(\frac{\overline{\mu_{\text{en}}}}{\rho} \right)_{\text{water}} . \quad (2)$$

This is a reasonable first approximation to the dose at dose maximum per unit incident photon fluence although the contribution of scattered photons may increase the value by several percent at high energies and a factor of two near 100 keV. Similarly, the difference between dose and kerma will increase the value slightly.

The surface dose in an electron beam can be determined using:

$$D_w = \phi \left(\frac{\overline{L}}{\rho} \right)_{\text{water}} \quad (3)$$

Note that because the stopping power is almost constant for the therapy energy range, the surface dose per unit incident fluence is almost constant. However, the fluence buildup means that the maximum dose is 15 to 30% greater than this value.

If one puts in the appropriate values, one finds that electron beams are more than an order of magnitude more effective at delivering dose per unit fluence. When one recalls that it takes many electrons from the accelerator to generate a photon at the patient plane, the electron beam current required for a photon beam is much greater than required for electron beams.

There are two ways to look at the results about the relative dose per unit fluence. For electron beams, every electron delivers dose at the surface of the phantom whereas for photons, the interactions are spread out throughout the phantom.

Another way to look at it is to consider an electron and a photon beam with the same energy fluence. The electron beam deposits all of the energy near the surface of the phantom (ignoring some minor backscatter and bremsstrahlung escaping). In contrast, anywhere from 30 to 60% of the photon beam passes right through a 30 cm patient or phantom while depositing the energy throughout the phantom. For a 10 MeV electron beam the energy is deposited in roughly a 5 cm slab whereas an equivalent photon beam (about 30 MV) would probably deposit no more than 40% of its energy in the phantom and spread that out over the 30 cm. Thus the difference in the dose delivered per unit incident fluence would be $10/4 \cdot 30/5 = 15$ (on average).

IV.A Dose and kerma per unit incident fluence

In an old paper I once calculated and tabulated the maximum absorbed dose to tissue per unit incident fluence and the water kerma per unit fluence for a range of photon energies.¹⁷ Values for a few photon energies are given in table II. Table III presents the maximum absorbed dose to water per unit incident fluence for broad parallel beams of electrons incident on a flat water phantom. These same data are presented in figure 42.

Table II: Maximum absorbed dose to ICRU 4-element tissue per unit incident photon fluence (in units of $(10^{-13}\text{Gy}\cdot\text{cm}^2)$) in a 30 cm thick slab of tissue irradiated by a broad parallel beam of photons and the water kerma per unit fluence at the same energies. Note that the difference between the dose to tissue and the dose to water is about 1% or less. From ref.¹⁷

photon energy MeV	maximum dose to tissue/fluence $10^{-13}\text{Gy}\cdot\text{cm}^2$	water kerma/fluence
0.010	54.0	76.7
0.020	16.8	16.4
0.100	7.33	4.10
0.500	31.8	26.4
1.00	54.9	49.5
5.00	155.	153.
10.00	243.	252.
20.00	416.	436.

Table III: Maximum absorbed dose to water per unit incident fluence (in units of $(10^{-10}\text{Gy}\cdot\text{cm}^2)$) in a 30 cm thick slab of water irradiated by a broad parallel beam of electrons. From ref.¹⁷

electron energy MeV	maximum absorbed dose to water/fluence $10^{-10}\text{Gy}\cdot\text{cm}^2$
0.100	19.4
0.200	12.2
0.500	7.70
1.00	6.18
2.00	5.31
5.00	4.68
10.0	4.22
20.0	3.79
30.0	3.57

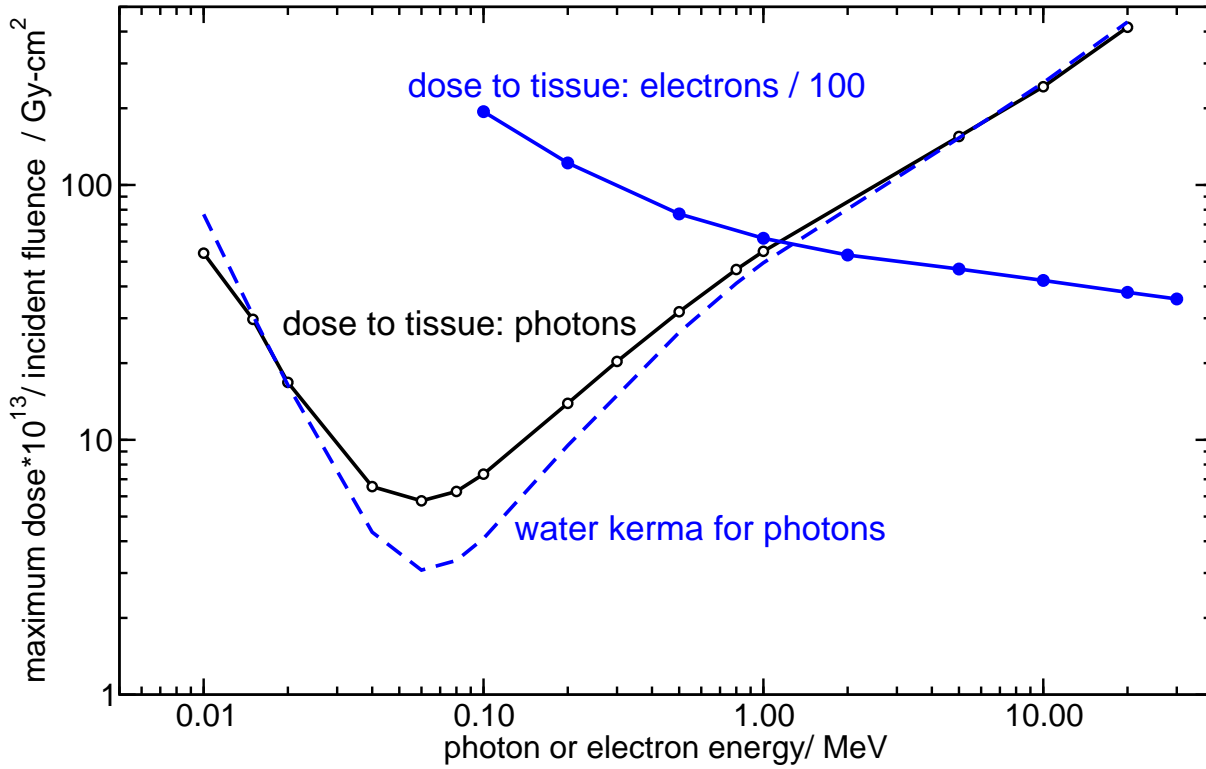


Figure 42: Maximum absorbed dose to ICRU 4-element tissue per unit incident fluence for broad parallel beams of photons and electrons as well as the ICRP21 values of the collision kerma approximation for photon beams. Note that the values for electron beams have been divided by 100. Data from ref.¹⁷

V Equivalent squares

There are a variety of different field shapes used in radiotherapy. In many situations it is necessary to know the depth-dose characteristics of the field actually used in the clinical situation and rather than measure it in every situation, it is useful to have methods to determine the depth-dose curve based on a smaller set of measured depth-dose curves. This is the goal of determining equivalent square fields. A square field of width a_{eq} is said to be equivalent to a rectangular or circular field if both beams have the same central-axis depth-dose characteristics. In modern practice the treatment planning system may provide similar information, but the equivalent square method provides a method of making a quick check.

The types of fields usually found in clinical practice (ignoring IMRT treatments) are:

square, rectangular: these can be on or off-axis and can be defined by the photons jaws on the accelerator.

circular: there may be special collimators, eg for stereotactic radiosurgery.

irregular: from custom shielding and now more commonly from MLCs.

V.A Rectangular fields

Figure 43 shows three rectangular or square field shapes which have the same central-axis depth-dose characteristics.

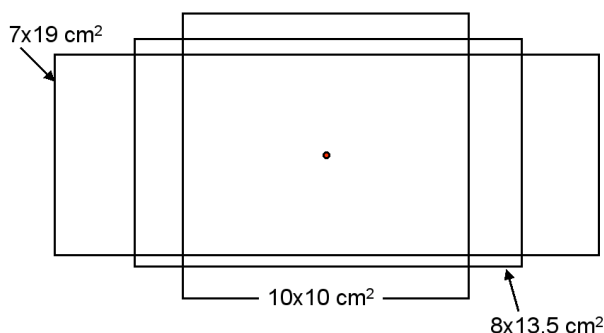


Figure 43: Two rectangles for which the central axis depth-dose characteristics are the same as for the $10 \times 10 \text{ cm}^2$ square field (from the data in BJR Supplement 25,¹⁸ some of which are presented in figure 44.)

Figure 44 presents data from BJR Supplement 25¹⁸ which can be used to determine equivalent square fields for various rectangular fields.

Aside from using pre-computed data such as in figure 44, there are several approaches to determining the size of an equivalent square field. The simplest approach is to find the square field with the same ratio of area to perimeter, *i.e.*:

$$\frac{ab}{2(a+b)} = \frac{a_{eq}^2}{4a_{eq}}, \quad (4)$$

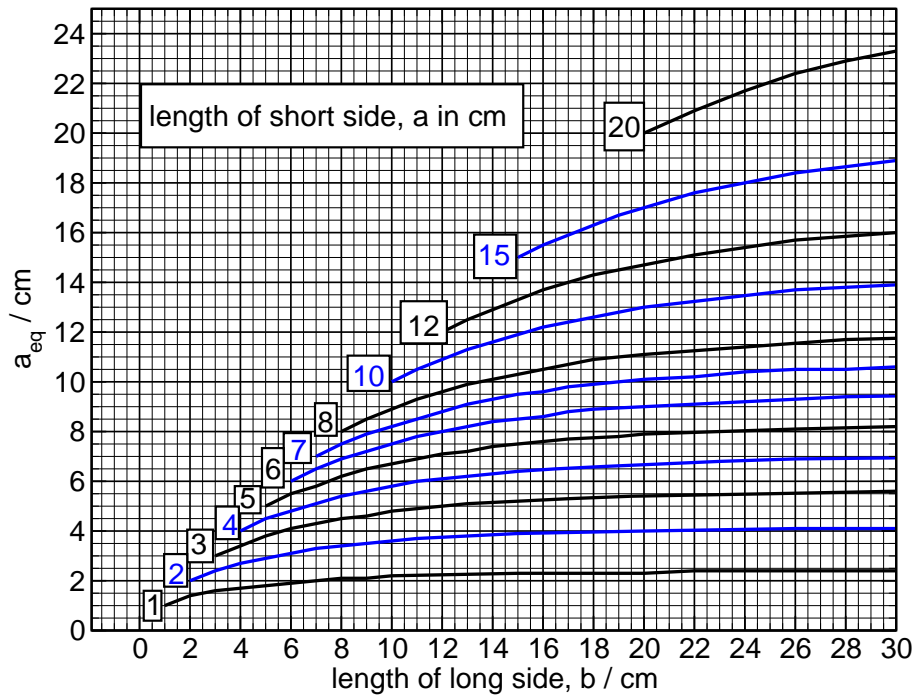


Figure 44: The length of the side of a square field, a_{eq} , which is equivalent to a rectangular field $a \times b \text{ cm}^2$ ($b > a$). Data taken from BJR Supplement 25¹⁸ or BJR Supplement 11 which is identical,¹⁹

and hence:

$$a_{eq} = \frac{4ab}{2(a+b)} = \frac{4 \times \text{area}}{\text{perimeter}} = \frac{4A}{P}. \quad (5)$$

This rule is generally ascribed to Sterling et al.²⁰

According to BJR25,¹⁸ this formula works well for $a < b \leq 20 \text{ cm}$ and $b/a \leq 4$. The maximum disagreement with their tables is said to be 3 mm which leads to an error in the depth-dose curves of less than 0.5% for ^{60}Co and higher energy beams. Fig 45 compares the BJR data to the results of the simple formula.

Asp²¹ used a treatment planning system to calculate the equivalent squares and demonstrated that the BJR results matched the $4A/P$ rule.

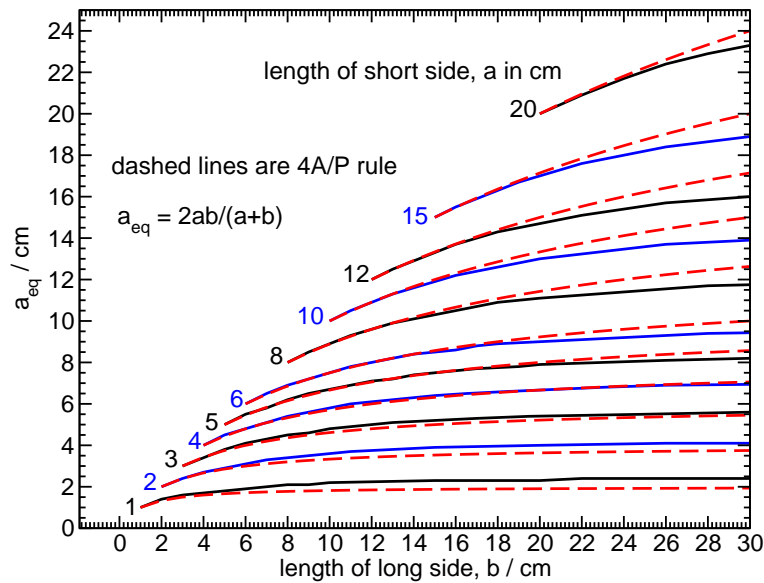


Figure 45: The length of the side of a square field, a_{eq} , which is equivalent to a rectangular field $a \times b$ cm² ($b > a$). Data taken from BJR Supplement 25¹⁸ are compared to the 4A/P rule given by Eq.(5).

V.B Circular fields

The simplest prescription for square and circular fields to be equivalent is if they have the same area, *i.e.*:

$$a_{eq}^2 = \pi r_{eq}^2 \quad (6)$$

and hence

$$a_{eq} = r_{eq} \sqrt{\pi} = 1.773 r_{eq}. \quad (7)$$

However, BJR25 gives the following formula as a more accurate relationship (their eqn(1), p138¹⁸):

$$a_{eq} = 1.782 r_{eq} + 0.0018 r_{eq}^2. \quad (8)$$

and conversely, their eqn(2)

$$r_{eq} = 0.5615 a_{eq} - 0.00034 a_{eq}^2. \quad (9)$$

How much do these formulae differ? Consider a circular beam with a radius of 5.640 cm. Eq.(7) gives $a_{eq} = 10$ cm whereas Eq.(8) give $a_{eq} = 10.11$ cm. This is a 1.1% difference in the side of the equivalent square. This has a negligible effect on the depth-dose curve. For example, the 10% change in field size going from a 9 cm field to a 10 cm field for a ⁶⁰Co beam at SSD = 100 cm causes the %dd(10) to change from 57.9% to 58.7% and hence the change from 10 to 10.11 cm will cause a correspondingly smaller change in the depth-dose curve.

Note that the 4A/P rule (which implies $a_{eq} = 2r_{eq}$) does not work for circular fields.

VI Effects of bin size on Monte Carlo calculated depth-dose curves

When calculating depth-dose curves with a Monte Carlo code, one is actually determining the dose averaged over a bin of finite width, Δz . In other words we calculate:

$$D_{MC}(z_0) = \frac{1}{\Delta z} \int_{z_0 - \frac{\Delta z}{2}}^{z_0 + \frac{\Delta z}{2}} D(z) dz. \quad (10)$$

If $D(z)$ is a constant, this reduces to $D_{MC}(z_0) = D(z)$, the average is just equal to the constant value. However, if $D(z)$ is varying, Kawrakow²² points out that:

$$D_{MC}(z_0) = D(z_0) \left[1. + \frac{D''(z_0)(\Delta z)^2}{24D(z_0)} + \dots + O((\Delta z)^4) \right], \quad (11)$$

where $D_{MC}(z_0)$ is the average dose in the bin of width (Δz) centered a z_0 , $D(z_0)$ is the dose at the mid-point of the bin, and $D''(z_0)$ is the second derivative at z_0 of the dose with respect to depth. This equation is derived using a Taylor expansion of the dose ($D(z) = D(z_0) + D'(z_0)\Delta z + \frac{1}{2!}D''(z_0)(\Delta z)^2 + \dots$) in eqn 10 and a great deal of algebra (at least in my straight forward derivation of it).

This equation tells us that for any depth-dose curve where the rate of change is constant, the dose at the middle of the bin is almost exactly equal to the average dose over the bin. However, in the build-up region the second derivative is not zero and so one must use small bins to ensure that this is the case.

Chad Hunter²³ looked at pure photon beam depth-dose curves and found that bins as small as 0.2 mm are sometimes required to get 0.1% accuracy in the buildup region of calculated depth-dose curves.

VI.A Problems

1. (a) Assume that the dose past dose maximum in a photon beam is given by $D(z) = D_0 e^{-\mu'z}$, and that in a particular beam the dose drops from 10 to 5.5 Gy going from 10 cm depth to 20 cm depth. What is the maximum bin width one can use in a Monte Carlo calculation to ensure that the average dose in the bin is within 0.1% of the dose at the mid-point in the bin?
- (b) Assuming that the bin width is close to the maximum width, are there other concerns with just joining the mid-points of the bins with straight lines and assuming that these lines give the dose at each point within the 0.1% limit?

References

- ¹ D. W. O. Rogers, I. Kawrakow, J. P. Seuntjens, and B. R. B. Walters, NRC User Codes for EGSnrc, Technical Report PIRS-702, National Research Council of Canada, Ottawa, Canada, 2000.
- ² I. Kawrakow, Accurate condensed history Monte Carlo simulation of electron transport. I. EGSnrc, the new EGS4 version, *Med. Phys.* **27**, 485 – 498 (2000).
- ³ I. Kawrakow and D. W. O. Rogers, The EGSnrc Code System: Monte Carlo simulation of electron and photon transport, Technical Report PIRS-701, National Research Council of Canada, Ottawa, Canada, 2000.
- ⁴ F. H. Attix, *Introduction to Radiological Physics and Radiation Dosimetry*, Wiley, New York, 1986.
- ⁵ E. Mainegra-Hing, D. W. O. Rogers, and I. Kawrakow, Calculation of energy deposition kernels for photons and dose point kernels for electrons, *Med. Phys.* **32**, 685 – 699 (2005).
- ⁶ D. W. O. Rogers and A. F. Bielajew, Calculated buildup curves for photons with energies up to ^{60}Co , *Med. Phys.* **12**, 738 – 744 (1985).
- ⁷ K. E. Sixel and E. B. Podgorsak, Buildup region and depth dose maximum of megavoltage x-ray beams, *Med. Phys.* **21**, 411 – 416 (1994).
- ⁸ B. R. Muir, G. Xiong, T. P. Selvam, and D. W. O. Rogers, ^{60}Co phase-space files generated using BEAMnrc, Technical Report CLRP 09-01, Carleton Laboratory for Radiotherapy Physics, Carleton University, Ottawa K1S 5B6, Canada, 2009.
- ⁹ Central axis depth dose data for use in radiotherapy: 1996, *Brit. J. Radiol., Suppl* **25**, 1 – 188 (1996).
- ¹⁰ R. Loevinger, A formalism for calculation of absorbed dose to a medium from photon and electron beams, *Med. Phys.* **8**, 1 – 12 (1981).
- ¹¹ D. Sheikh-Bagheri and D. W. O. Rogers, Monte Carlo calculation of nine megavoltage photon beam spectra using the BEAM code, *Med. Phys.* **29**, 391 – 402 (2002).
- ¹² R. Mohan, C. Chui, and L. Lidofsky, Energy and angular distributions of photons from medical linear accelerators, *Med. Phys.* **12**, 592 – 597 (1985).
- ¹³ G. Mora, A. Maio, and D. W. O. Rogers, Monte Carlo simulation of a typical ^{60}Co therapy source, *Med. Phys.* **26**, 2494 – 2502 (1999).
- ¹⁴ D. W. O. Rogers and A. F. Bielajew, 20 MeV electrons on a slab of water, in *Monte Carlo Transport of Electrons and Photons*, edited by T. M. Jenkins, W. R. Nelson, A. Rindi, A. E. Nahum, and D. W. O. Rogers, pages 139 – 152, Plenum Press, New York, 1988.
- ¹⁵ D. Harder, *High Energy Electrons (Proc. Symp. Berlin, 1964)*, Springer-Verlag, Berlin, 1965.

- ¹⁶ G. X. Ding, D. W. O. Rogers, and T. R. Mackie, Mean energy, energy-range relationship and depth-scaling factors for clinical electron beams, *Med. Phys.* **23**, 361 – 376 (1996).
- ¹⁷ D. W. O. Rogers, Fluence to Dose Equivalent Conversion Factors Calculated with EGS3 for Electrons from 100 keV to 20 GeV and Photons from 20 keV to 20 GeV, *Health Physics* **46**, 891 – 914 (1984).
- ¹⁸ M. J. Day and E. G. A. Aird, Appendix A: The equivalent field method for dose determinations in rectangular fields, *Brit. J. Radiol., Suppl* **25**, 138 – 151 (1996).
- ¹⁹ M. J. Day, Appendix A: The equivalent field method for axial dose determinations in rectangular fields, *Brit. J. Radiol., Suppl* **11**, 95 – 100 (1972).
- ²⁰ T. D. Sterlin, H. Perry, and L. Katz, Automation of radiation treatment planning, IV, *Brit. J. Radiol.* **37**, 544 – 550 (1964).
- ²¹ L. W. Asp, On equivalent square fields, *Brit. J. Radiol.* **53**, 485 – 487 (1980).
- ²² I. Kawrakow, On the effective point of measurement in megavoltage photon beams, *Med. Phys.* **33**, 1829 – 1839 (2006).
- ²³ C. R. Hunter, Monte Carlo Simulation Of Depth Dose Curves And Humidity Correction Factors For The $^{90}\text{Sr}^{90}\text{Y}$ Beta Radiation Source, Carleton University Honours Project Report, Physics Dept , 1–59 (2007).